

February 8, 2020

Higgs Mass Determination from Direct Reconstruction at a Linear e^+e^- Collider

AURELIO JUSTE

Fermi National Accelerator Laboratory,
P.O. Box 500, MS 357,
Batavia, IL 60510,
Phone: 1 (630) 840-6565 Fax: 1 (630) 840-8481
e-mail: juste@fnal.gov

Abstract

We study the feasibility of a precise measurement of the mass of a 120 GeV MSM Higgs boson through direct reconstruction of $ZH \rightarrow q\bar{q}H$ events that would be achieved in a future e^+e^- linear collider operating at a center-of-mass energy of 500 GeV. Much effort has been put in a “realistic simulation” by including irreducible and reducible backgrounds, realistic detector effects and reconstruction procedures and sophisticated analysis tools involving Neural Networks and kinematical fitting. As a result, the Higgs mass is determined with a statistical accuracy of 50 MeV and the Z-Higgs Yukawa coupling measured to 0.7%, assuming 500 fb⁻¹ of integrated luminosity.

Results presented at the International Workshop on Linear Colliders (LCWS99)
Sitges, Barcelona, Spain, 28 April - 5 May 1999

1 Introduction

The Standard Model [1] (MSM) of electroweak and hadronic interactions has been successfully tested so far to an extremely high degree of accuracy. However, one of its key elements, the Higgs mechanism, remains to be tested experimentally. It is through the interaction with the ground state Higgs field that the fundamental particles acquire mass, which in turn sets the scale of the coupling with the Higgs boson. Once the Higgs boson is found, all its properties have to be accurately measured. In the MSM, the Higgs mass is not predicted by the theory but the profile of the Higgs particle: decay width, branching ratios and production cross-section, are uniquely determined once M_H is fixed, hence the importance of performing a precise measurement of the Higgs mass. In order to establish experimentally that this particle has indeed the properties of a Higgs boson, we need to prove that it is a scalar particle and that it arises from a field with a vacuum expectation value which contributes to the W and Z masses [2]. The latter is achieved by determining the Higgs Yukawa couplings to the Z and W gauge bosons, which in an e^+e^- collider can be measured from the Higgstrahlung process: $Z^* \rightarrow ZH$ [3] and the fusion processes: W^*W^* , $Z^*Z^* \rightarrow H$ [4]. The scalar nature of this particle can be verified from its production angular distribution.

In this work we have assumed that the MSM Higgs boson in the “Intermediate Mass Region” ($M_Z \leq M_H \leq 2M_W$) will have already been discovered at the present (LEP2, TeVatron) or future (LHC, NLC) accelerators, and study the feasibility of a precise measurement of its mass and Yukawa coupling to the Z boson from the Higgstrahlung process.

This mass range is favored both experimentally: from global fits to electroweak precision observables at LEP, SLC and TeVatron the upper limit $M_H < 260$ GeV at 95% CL [5] is derived, whereas from direct search at LEP2 $M_H > 95.2$ GeV at 95% CL [6]; and theoretically: the stability and triviality bounds constrain the MSM Higgs boson mass to be in the range $130 \text{ GeV} \leq M_H \leq 180 \text{ GeV}$ [7]. A Higgs boson in the “Intermediate Mass Region” would be relatively more difficult to detect at LHC than a heavy Higgs: whereas a Higgs boson in the mass range 150-700 GeV can be found straightforwardly in the decay $H \rightarrow ZZ \rightarrow 4\ell$, the discovery of the light MSM Higgs boson would be based on $H \rightarrow \gamma\gamma$ and would require 100 fb^{-1} of data (a year’s running at the design luminosity). Instead, a light Higgs boson might be discovered with less than 1 fb^{-1} of integrated luminosity at a future e^+e^- linear collider operating at $\sqrt{s} = 300$ GeV [8]. However, the job of a linear e^+e^- collider would be rather to study in great detail the properties of the Higgs particle, which can be uniquely be attained in the clean and very high luminosity ($\int \mathcal{L} dt \geq 100 \text{ fb}^{-1}/\text{year}$) environment expected.

As already mentioned, we will focus on the case of the MSM Higgs boson, which is equivalent, for $M_H \leq 130$ GeV, to the case of the light h MSSM Higgs boson close to the decoupling regime (where the MSM and MSSM Higgs sectors look practically the same). For the sake of definiteness, we will assume $M_H = 120$ GeV and concentrate on the Z hadronic decay mode: $e^+e^- \rightarrow ZH \rightarrow q\bar{q}H$. For $M_H = 120$ GeV, the Higgs decays dominantly to $b\bar{b}$ ($\text{BR}(H \rightarrow b\bar{b}) \simeq 72\%$), which leads to multi-jet event topologies involving at least 2 b -jets in the final state. Therefore, one of the crucial experimental aspects will be flavor tagging. Most of previous studies have been focussed on the leptonic Z decay

mode since it is less affected by background and there is a better intrinsic resolution on M_H (through the recoil mass distribution). For instance, in [15] a statistical uncertainty of $(\Delta M_H)_{stat} \simeq 110$ MeV is obtained from the combination of $ZH \rightarrow e^+e^-H$, $\mu^+\mu^-H$ channels at $\sqrt{s} = 350$ GeV and assuming 500 fb^{-1} of integrated luminosity. The disadvantage is the lack of statistics ($BR(Z \rightarrow \ell^+\ell^-) \simeq 10\%$) as compared to the hadronic decay channel ($BR(Z \rightarrow q\bar{q}) \simeq 70\%$). Therefore, it is fully justified to investigate to what extent it is possible to make of the hadronic decay channel a competitive measurement.

2 Experimental Strategy

As already mentioned, the main production mechanisms of the MSM Higgs boson in e^+e^- annihilation are the Higgstrahlung process: $e^+e^- \rightarrow Z^* \rightarrow ZH$ (with a cross-section scaling as $1/s$ and therefore dominating at low energy) and WW -fusion: $e^+e^- \rightarrow \nu\bar{\nu}W^*W^* \rightarrow \nu\bar{\nu}H$ (which dominates at high energies since the cross-section scales as $\log(s/M_H^2)$). One order of magnitude smaller than WW -fusion there is also the contribution from ZZ -fusion: $e^+e^- \rightarrow e^+e^-Z^*Z^* \rightarrow e^+e^-H$. At $\sqrt{s} = 500$ GeV and for $100 \text{ GeV} \leq M_H \leq 200 \text{ GeV}$, the Higgstrahlung and WW -fusion have approximately the same cross-section.

The lowest order total cross-section for ZH , assuming $M_H = 120$ GeV, is shown in Fig. 1 as a function of the center-of-mass energy. The effect of radiative processes in the initial state (initial state radiation¹ and beamstrahlung) on the total cross-section is also illustrated. The total cross-section at $\sqrt{s} = 500$ GeV is about 66 fb, which represents an event sample of about 6600 events/year assuming² $\mathcal{L} = 10^{34} \text{ cm}^{-2}\text{s}^{-1}$.

The measurement is performed at $\sqrt{s} = 500$ GeV. In principle, one would prefer to sit at the peak of σ_{ZH} :

$$(\sqrt{s})_{peak} \simeq M_Z + \sqrt{2}M_H,$$

that is $(\sqrt{s})_{peak} \simeq 260$ GeV for $M_H = 120$ GeV, since the cross-section is enhanced by a factor $\simeq 3.4$ with respect to $\sqrt{s} = 500$ GeV and the background from $t\bar{t}$ is not present. However, it is unclear how feasible it would be to collect enough integrated luminosity at such a low center-of-mass energy in order to perform a precise measurement. Therefore, a more realistic strategy could be to perform a first direct measurement of M_H at the $t\bar{t}$ threshold ($\sqrt{s} = 350$ GeV, where still $\sigma_{ZH}(350 \text{ GeV}) \simeq 2.1 \sigma_{ZH}(500 \text{ GeV})$) and contemporary with the top threshold measurements, and then perform the precise measurement at $\sqrt{s} \geq 500$ GeV, where most of the integrated luminosity will be collected.

There are two main strategies for the Higgs mass measurement:

- calculation of the mass recoiling against the Z : this has the nice feature of being independent on assumptions about the Higgs decay modes [15], and would show the Higgs resonance even for invisible Higgs decays. The recoil mass is computed from the reconstructed Z 4-momentum assuming the nominal center-of-mass energy:

$$M_H^2 = s - 2\sqrt{s}E_Z + M_Z^2, \quad (2.1)$$

¹Initial state radiation will be used hereafter as synonymous with bremsstrahlung.

²It has been assumed that 1 year's running = 10^7 s.

where E_Z and M_Z are, respectively, the Z reconstructed energy and invariant mass. Therefore, this method is more suitable for the Z leptonic decay channel since a more precise Z reconstruction is possible.

- direct reconstruction of the invariant mass of the Higgs decay products. As will be shown, this method works better for hadronic Z decays than the recoil mass method.

The total cross-section depends sensitively on the Z-Higgs Yukawa coupling, which can thus be inferred from the comparison of the measured total cross-section with the theoretical expectation as a function of g_{ZZH} . Therefore it is possible to verify whether this field is the responsible for the whole Z mass (as in the MSM), or only for a fraction of it.

3 Simulation Aspects

The signal and the different backgrounds have been generated with PYTHIA [9]. The top quark and Higgs masses have been assumed to be $m_t = 175$ GeV and $M_H = 120$ GeV, respectively. Interference between signal and background have been neglected. The event samples have been generated at $\sqrt{s} = 500$ GeV, including initial state radiation (ISR) and beamstrahlung. For efficiency reasons, a generation cut $\sqrt{s'} > 100$ GeV has been applied. Initial state radiation has been considered in the structure function approach and beamstrahlung has been generated with the aid of the CIRCE program [10]. Fragmentation, hadronization and particles' decays are handled by JETSET [9], with parameters tuned to LEP2 data.

3.1 Detector Simulation

Once the events have been generated, they are processed through a fast simulation [11] of the response of a detector for a future linear collider. The detector components, which are assumed to be:

- a vertex detector,
- a tracker system with main tracker (2 m. radius TPC embedded in a 2 Tesla magnetic field), forward tracker and forward muon tracker,
- an electromagnetic calorimeter,
- a hadronic calorimeter and
- a luminosity detector,

are implemented according to the Large Detector model in [12].

This fast detector simulation provides a flexible tool since its performance characteristics can be varied within a wide range. The calorimeter response is treated in a realistic way using a parametrization of the electromagnetic and hadronic shower deposits obtained from a full GEANT simulation [13] and including a cluster finding algorithm.

Pattern recognition is emulated by means of a complete cross-reference table between generated particles and detector response. The output of the program consists of a list of reconstructed objects: electrons, gammas, muons, charged and neutral hadrons and unresolved calorimeter clusters, as a result of an idealized Energy Flow (EF) algorithm incorporating track-cluster matching.

3.2 B-tagging

Jets coming from b and c -quark decays are tagged based on the non-zero lifetime of these quarks, using the Vertex Detector (VDET). In this study we have assumed the performance of a CCD VDET in a 1 cm radius beampipe.

In order to look for this lifetime signal, we have chosen to use the 3D impact parameter (IP) of each charged track (distance of closest approach between the track and the b production point). Since the statistical resolution of the IP varies strongly from one track to another, we use the estimated statistical significance of the measured IP to define our tag. The b -tagging algorithm is kept simple so that the success of the analysis does not depend on detector details. More efficient algorithms can be developed by making use of multivariate techniques, such as Neural Networks.

In Fig. 3, the IP significance distributions for different Z hadronic decays are compared. The lifetime signature can be clearly seen for $Z \rightarrow b\bar{b}$ in the positive tail. We will use the IP distribution for prompt tracks (those originated from $Z \rightarrow u\bar{u}, d\bar{d}, s\bar{s}$) to define, for each track, a probability “to be consistent with originating from the primary vertex”. This information can then be combined to get a probability per jet or for the whole event [14].

In order to test the performance of such b -tagging, we have estimated its efficiency and purity for a given definition of b -jet. To do so, the Monte Carlo generated quarks are assigned to the reconstructed jets by a matching algorithm which associates those quark-jet pairs with minimum invariant mass, starting from the most energetic quark. In order not to reduce drastically the signal efficiency, we will not use the number of found b -jets for a certain lifetime probability as a selection cut. Instead, for every event, we will define as b -jets those two with the lowest probability (to originate from the primary vertex). Applied to $ZH \rightarrow q\bar{q}b\bar{b}$ (with $q = u, d, s, c, b$) events, this algorithm would tag the two correct H b -jets in $\sim 43\%$ of the cases, and at least one of them in $\sim 93\%$ of the cases.

4 Experimental Analysis

The experimental analysis is performed assuming a total integrated luminosity of 10 fb^{-1} , which can be collected in around 11 days of running at $\mathcal{L} = 10^{34} \text{ cm}^{-2}\text{s}^{-1}$.

In spite of the apparently clean signature of this decay channel (4 jets in the final state, out of which ≥ 2 are b -jets, di-jet invariant mass constraint for the Z decay, etc), the measurement has many difficulties, among which are:

- the tiny signal ($\sigma_{ZH \rightarrow q\bar{q}H} \simeq 46.2 \text{ fb}$) with backgrounds about 300 times larger: in Table 1, the total cross-sections for the signal and different backgrounds considered

are listed together with the numbers of generated events;

- limitations of jet-clustering algorithms in properly reconstructing 4 jets in the final state due to hard gluon radiation, jet-mixing, etc;
- degradation of b -tagging performance due to hard gluon radiation;
- missing energy in b jets from neutrino emission. For instance, the branching ratio for semileptonic+leptonic decay modes of the B^\pm is $\simeq 52.4\%$.

Process	σ (fb)	Generated events
$ZH \rightarrow q\bar{q}H$	46.2	100k
$ZH \rightarrow \ell^+\ell^-H$	6.7	100k
$q\bar{q}$ (5 flavors)	3860.4	1M
$t\bar{t}$	582.0	1M
W^+W^-	7821.4	2.2M
ZZ	570.0	1M

Table 1: Total cross-section for signal and the different backgrounds considered at $\sqrt{s} = 500$ GeV. Initial state radiation and beamstrahlung have been included. For efficiency reasons, a generation cut of $\sqrt{s'} > 100$ GeV has been applied. Also listed is the number of generated events for every process.

Due to the very small signal-to-background (S/B) ratio, the philosophy of the analysis will be to start by applying a standard-cuts preselection in order to remove as much background as possible while keeping a high efficiency for the signal. Then, in order to further improve the statistical sensitivity to the signal, a multivariate analysis will be performed. At this stage our problem will be how to make an optimal use of the statistical information from a set of N distributions discriminating between signal and background. It can be proven [16] that it is possible to make an optimal projection from the input N -D space to a 1-D space³:

- a) without loss of sensitivity on the classes proportions and
- b) with a probabilistic interpretation (in terms of the a-posteriori Bayesian probability of being of signal type).

This projection can be performed by using Neural Network (NN) techniques, which have become increasingly popular in High Energy Physics in the last few years.

³In the general case of m existing classes to be discriminated, the optimal projection is performed in a space $(m - 1)$ -dimensional. In our problem, all backgrounds are considered inclusively and $m = 2$, thus the optimal projection is 1-dimensional.

4.1 Event Selection

As already mentioned, a standard cuts preselection is applied in order to remove as much background as possible before the multivariate analysis. The selected events are required to have a visible mass in excess of $0.6\sqrt{s}$ (i.e. 300 GeV), more than 40 EF objects reconstructed, at least 4 jets reconstructed with the JADE [17] jet-clustering algorithm with a resolution parameter $y_{cut} = 4 \times 10^{-3}$ and a thrust value ranging in between 0.85 and 0.925. Next, the event is forced to have exactly 4 jets reconstructed using the JADE algorithm. Further preselection cuts require a minimum of 2 charged tracks per jet and a minimum di-jet invariant mass of 40 GeV. The preselection variables are compared for signal and background in Fig. 4, along with the cuts applied. The preselection efficiencies and effective cross-sections for the different processes considered are listed in Table 2. After preselection, the efficiency for signal is reduced to 67.3% and the sample purity is only $\simeq 4.0\%$.

Process	ϵ (%)	σ_{eff} (fb)
$ZH \rightarrow q\bar{q}H$	67.27	31.08
$ZH \rightarrow \ell^+\ell^-H$	1.48	0.10
$q\bar{q}$ (5 flavors)	6.76	290.96
$t\bar{t}$	4.26	24.79
W^+W^-	5.00	391.07
ZZ	12.30	70.11
<i>Total Bckg</i>		747.03

Table 2: Hadronic channel preselection efficiencies and effective cross-sections.

As it can be observed in Fig. 4, the preselection variables after cuts still have discriminant power between signal and background. In order to optimally use these variables, they are further used together with three more variables to train a Preselection NN. These three variables (shown in Figs. 5a, 5b and 5c) provide information about the lifetime content of the event: the logarithm of the event probability to contain no-lifetime, the difference between the probability of the second jet and the first jet (sorted from the most b -like to the least b -like) and the number of b -jets found (where a b -jet is defined as a jet with a no-lifetime probability smaller than 13.5%). In Fig. 5d it is shown the Preselection NN output, after training, for both signal and background. No cut is applied in this distribution, but it is rather used as a discriminant variable.

There are 12 more variables which are discriminant between signal and background (see Figs. 6 and 7). Most of them are variables about the global event topology:

- Evis: total visible energy of the event;
- Max(Ejet)-Min(Ejet): difference between maximum and minimum jet energy;
- Njets(LUCLUS, $d_{cut}=20$ GeV): number of jets found with the LUCLUS [18] jet-clustering algorithm for a distance measure of 20 GeV;

- low jet mass of the event. The event is divided in two hemispheres and particles are assigned to either hemisphere in order to minimize the quadratic sum of the two hemispheres invariant mass (hereafter called respectively high and low jet masses). For processes with two resonances (such as W^+W^- , ZZ or ZH), these distributions tend to show resonant structures around the true invariant masses.
- minimum di-jet angle;
- cosine of the polar angle of the thrust axis;
- normalized Fox-Wolfram moments h_{30} and h_{40} ;
- aplanarity,
- number of hard leptons ($E > 50$ GeV) found;

others contain information about flavor tagging (sum of the no-lifetime probability for the two most b -like jets) or Z invariant mass reconstruction (see Sect. 4.2).

These variables, together with the Preselection NN output (PreselNNO) distribution are used to train a Selection NN. Table 3 shows the discriminant power of each of the 13 variables used in the Selection NN. The Selection NN output (SelNNO) distribution is compared for signal and background in Fig. 8a. In Fig. 8b, the signal efficiency (ϵ) and purity (ρ) as a function of the cut in the SelNNO are shown. Among the different backgrounds, the main contribution in the “signal region” (e.g. SelNNO > 0.85) comes from $q\bar{q}$ (5 flavors), followed by ZZ , as shown in Fig. 9.

Variable	Discriminant Power (%)
$\max(E^{\text{jet}}) - \min(E^{\text{jet}})$	8.8
$\min(\theta_{ij})$	7.6
$N_{\text{jets}}(\text{LUCLUS})$	5.2
$P_{\text{btagOrd}}^{\text{jet1}} + P_{\text{btagOrd}}^{\text{jet2}}$	4.1
$\cos(\Theta_T)$	6.0
h_{30}	11.0
h_{40}	9.1
Low jet mass	8.2
M_Z^{reco}	9.8
Number of hard leptons	4.3
E_{vis}	9.9
Aplanarity	7.2
PreselNNO	8.7

Table 3: Discriminant power of each of the 12 input variables of the Selection NN.

The selection can be performed in such a way as to minimize the statistical uncertainty in the cross-section measurement and thus, in the Z-Higgs Yukawa coupling:

$$\left(\frac{\Delta g_{ZZH}}{g_{ZZH}}\right)_{stat} = \frac{1}{2} \left(\frac{\Delta \sigma_{ZH}}{\sigma_{ZH}}\right)_{stat} = \frac{1}{2} \frac{1}{\sqrt{\sigma_{ZH \rightarrow q\bar{q}H}}} \frac{1}{\sqrt{\epsilon \rho L}},$$

where L is the integrated luminosity. This cut would correspond to the maximum of $\epsilon \rho$ shown in Fig. 8b, $(\epsilon \rho)_{max} \simeq 0.23$, which translates into:

$$\left(\frac{\Delta \sigma_{ZH}}{\sigma_{ZH}}\right)_{stat} \simeq 9.7\%, \quad \left(\frac{\Delta g_{ZZH}}{g_{ZZH}}\right)_{stat} \simeq 4.9\%,$$

assuming 10 fb^{-1} of integrated luminosity⁴. This optimal cut, $\text{SelNNO} > 0.85$, leads to a signal efficiency of 38.0% and a purity of 56.2%. The selection efficiencies and effective cross-sections for the different backgrounds are given in Table 4, corresponding to the above cut. However, in order to determine the Higgs mass, a higher sample purity is in general desirable, which can be obtained by performing a tighter cut on SelNNO.

Process	ϵ (%)	σ_{eff} (fb)	# Events (L=10 fb ⁻¹)
$ZH \rightarrow q\bar{q}H$	38.0	17.56	176
$ZH \rightarrow \ell^+ \ell^- H$	~ 0	~ 0	~ 0
$q\bar{q}$ (5 flavors)	1.30×10^{-1}	5.02	50
$t\bar{t}$	3.92×10^{-1}	2.28	23
W^+W^-	3.40×10^{-2}	2.66	27
ZZ	6.50×10^{-1}	3.70	37
<i>Total Bckg</i>		13.66	137

Table 4: Selection efficiencies and effective cross-sections for $\text{SelNNO} > 0.85$.

4.2 Higgs mass reconstruction

Once the events have been selected, the Higgs invariant mass has to be reconstructed. In this analysis we are not going to be exclusive in the reconstruction of the different Higgs decay channels, but rather try to reconstruct always 4 jets in the final state. Indeed, this leads to some inefficiency (in particular for H decay modes such as $H \rightarrow W^+W^-, \tau^+\tau^-$), but since $BR(H \rightarrow b\bar{b} + c\bar{c} + gg) \simeq 80\%$, it is fully justified for the purpose of this study.

For four reconstructed jets in the final state there are 6 possible di-jet assignments. At this point we do not use the b -tagging information in order to identify the b -jets coming from the Higgs, nor any assumption about the Higgs mass. Instead, the combination which maximizes $\mathcal{P}(m_{ij} - m_Z)$, where m_{ij} is the invariant mass between jets i and j , and \mathcal{P} is the probability density function of the Z invariant mass for the correct jet pairing,

⁴A better statistical uncertainty could in principle be obtained from a likelihood fit to the SelNNO distribution.

is selected. The efficiency to tag the correct combination is 68% before preselection and goes up to 85% for the finally selected events. Therefore, the combinatorial background in the final Higgs invariant mass distribution is $\sim 15\%$.

As already mentioned, the raw recoil mass distribution from the reconstructed Z jets is not really suited for a precise M_H measurement in the hadronic channel, even assuming perfect knowledge of the event-by-event effective center-of-mass energy. Instead, the raw di-jet invariant mass distribution from the H jets shows a much sharper peak around 120 GeV, as shown in Fig. 10. The asymmetry and low mass tail for the the raw H di-jet invariant mass distribution is caused by energy losses in the H decays (dominated by neutrino emission in b decays from $H \rightarrow b\bar{b}$, but also receiving a small contribution from other H decay modes such as $\tau^+\tau^-$ or W^+W^-). This is demonstrated in Fig. 11, where the amount of energy lost in the form of neutrinos by each H jet has been computed at the hadron level from the MC. The fraction of energy lost is defined for each H jet with respect to the true H daughter's energy. Then, the sum of both fractions is required to be below 2% for an event to be considered with no missing energy in the H decay.

In order to improve the Higgs invariant mass resolution, a kinematical fit (KF) imposing energy and momentum conservation is performed. In an event-by-event basis, the whole event kinematics (represented in Fig. 12) is fitted:

- di-jet invariant masses: M_Z and M_H ;
- production angles of the Z boson in the e^+e^- rest frame: θ_Z and ϕ_Z ;
- production angles of one of the Z jets with respect to the Z direction in the Z rest frame: θ_q^* and ϕ_q^* ;
- production angles of one of the H jets with respect to the H direction in the H rest frame: θ_b^* and ϕ_b^* .

The jet masses have been fixed to the reconstructed values. In order to properly correct the jet energies and angles, we have included in the kinematical fit the non-gaussian probability density functions (PDFs):

$$f(E_q - E_j | E_q), \quad f(\theta_q - \theta_j | E_q), \quad f(\phi_q - \phi_j | E_q),$$

where $E_{q(j)}$, $\theta_{q(j)}$ and $\phi_{q(j)}$ are respectively the energy and angles of the quarks(jets) in the laboratory frame. This is particularly important for b -jets, as can be observed in Fig. 13. Therefore, the above PDFs have been parametrized separately for light-quark and b -jets.

In Fig. 13, the jet energy resolution is compared for light-quark jets from the Z and “ b -jets”⁵ from the H in 3 different quark energy ranges. The contribution from $H \rightarrow W^+W^-, \tau^+\tau^-$ has also been explicated. As it can be observed, at low parent quark energy the jet energy resolution distribution is very similar for both Z light-quark and H b -jets and shows a negative tail because of jet-mixing with the other jet from the same boson decay, whereas the mixing between jets belonging to different boson decay is negligible.

⁵As already mentioned, we have been inclusive in the treatment of H decay modes other than $b\bar{b}$ and they are included in the histograms.

The main reason is the large boost of the Z and H , which reduces the angular separation between the decay products belonging to the same boson:

$$\begin{aligned} \langle \theta_{jet \in H(Z), jet \in H(Z)} \rangle &\simeq 70^\circ (56^\circ), \\ \langle \min(\theta_{jet \in Z, jet \in H}) \rangle &\simeq 120^\circ. \end{aligned}$$

As the parent quark energy increases, the difference between the jet energy resolution for light-quark and b -jets becomes more evident, the latter developing a larger positive tail. The reconstructed jet energy is lower than the quark energy because of losses in neutrino emission, which are not however larger for jets coming from lower energy quarks, but which become more evident at high energy because of the better performance of the jet-clustering algorithm in properly reconstructing the jet. Fig. 14 shows the effect of jet-mixing and missing energy on the bi-dimensional distribution of energy resolution for both H jets (only $H \rightarrow b\bar{b}, c\bar{c}, gg$ decay channels have been included). As expected, jet energy losses are uncorrelated for both H jets, whereas jet-mixing introduces a clear anticorrelation. The jet-mixing is computed at the hadron level and defined as the fraction of the reconstructed jet energy coming for the other quark in the same boson decay.

In order to further improve the H invariant mass resolution, it is necessary to properly account for initial state radiation and beamstrahlung in the kinematical fit. As it can be observed in Fig. 15, it constitutes the second largest source of degradation in the H di-jet invariant mass resolution (the first one being energy losses in b -jet decays). In order to account for the event-by-event fluctuations in the effective center-of-mass energy and boost along the z -direction, the fraction of energy carried by the e^- and the e^+ : x_1 and x_2 , after ISR and beamstrahlung is fitted by including in the likelihood the ISR structure functions for both the e^- and e^+ . Indeed, it would be best to include the effective structure functions (after selection) accounting for ISR and beamstrahlung. However, even this simple approach gives good results, as it is shown in Fig. 16, where a clear correlation between the true and fitted total longitudinal momentum and the true and fitted effective center-of-mass energy is observed. Fig. 17 illustrates the overall improvement in the H invariant mass resolution by performing a kinematical fit with respect to the raw reconstructed di-jet invariant mass, as well as the further gain obtained by including ISR and beamstrahlung in the kinematical fit.

4.3 Higgs mass determination

The Higgs mass is determined from a likelihood fit to the H invariant mass distribution resulting from the kinematical fit (M_H^{KF}). The data sample corresponds to $\int \mathcal{L} dt = 10 \text{ fb}^{-1}$ and includes background (see Fig. 18b). The Higgs mass estimator for a particular data sample containing N_{data} events, \hat{M}_H , is obtained by maximizing the log-likelihood function:

$$\mathcal{L}(M_H) = -2 \log L(M_H) = -2 \sum^{N_{data}} \log \{ \rho \mathcal{P}_S(M_H^{KF} | M_H) + (1 - \rho) \mathcal{P}_B(M_H^{KF}) \} \quad (4.1)$$

where ρ is the expected signal purity and $\mathcal{P}_{S(B)}$ is the signal (background) PDF. The fit is performed in the range $115 \text{ GeV} \leq M_H^{KF} \leq 125 \text{ GeV}$, where most of the sensitivity to

M_H exists and the signal PDF is to a good approximation a truncated Breit-Wigner distribution with ~ 2.2 GeV width. Apart from the cut in the H invariant mass distribution, a selection cut $\text{SelNNO} > 0.9$ has been applied, leading to a signal efficiency of 16.5% and a purity of 82.1%. The expected numbers of signal and background events in the data sample are 76.2 and 13.6, respectively.

A number of MC experiments is performed and the expected error in the Higgs mass is computed as the RMS of the distribution of M_H estimators. The M_H estimator used has been checked to be unbiased by comparing the mean of the distribution of estimators with the input Higgs mass. The resulting statistical uncertainty on M_H is:

$$(\Delta \hat{M}_H)_{stat} \simeq 350 \text{ MeV},$$

corresponding to $\int \mathcal{L} dt = 10 \text{ fb}^{-1}$. The effect of the background contamination is a $\sim 7\%$ degradation in the statistical uncertainty. The effect of taking into account ISR and beamstrahlung in the kinematical fit has been a $\sim 20\%$ decrease in the statistical uncertainty.

5 Conclusions

In this work we have focussed on the feasibility of a precise measurement of the mass of a 120 GeV MSM Higgs boson by direct reconstruction, that would be attained at a high luminosity e^+e^- future linear collider operating at a center-of-mass energy of $\sqrt{s} = 500$ GeV.

In common with previous studies, we have considered the Higgstrahlung process: $e^+e^- \rightarrow Z^* \rightarrow ZH$, which constitutes the main Higgs production mechanism at $\sqrt{s} \leq 500$ GeV for $M_Z \leq M_H \leq 2M_W$. However, most results found in the literature have focussed on the Z leptonic decay channel: $ZH \rightarrow \ell^+\ell^-H$, due to the smaller background, the better intrinsic resolution on the Higgs invariant mass through the recoil mass distribution and the possibility of a measurement independent of assumptions about the Higgs decay modes.

Here we have rather concentrated on the Z hadronic decay channel: $ZH \rightarrow q\bar{q}H$, which has the bonus of a much larger statistics, but also the complications associated with a larger background, limitations of jet-clustering algorithms in properly reconstructing multi-jet final states, poor di-jet invariant mass resolution, etc. Much effort has been put in performing a “realistic simulation” by including irreducible and reducible backgrounds as well as realistic detector effects and reconstruction procedures. In order to fully exploit the possibilities of this decay channel, the use of sophisticated tools such as Neural Networks and kinematical fitting has been found to be important. As a result, the Higgs mass and Z -Higgs Yukawa coupling can be determined with a statistical accuracy exceeding that of the Z leptonic decay channel. For illustrative purposes only, the results of a recent study [15] making use of $ZH \rightarrow \ell^+\ell^-H$, $\ell = e, \mu$ events at $\sqrt{s} = 350$ GeV have been naively rescaled to $\sqrt{s} = 500$ GeV and compared to the results from this work:

$$ZH \rightarrow \ell^+\ell^-H, \ell = e, \mu : \quad (\Delta M_H)_{stat} \simeq 160 \text{ MeV}, \quad \left(\frac{\Delta g_{ZZH}}{g_{ZZH}} \right)_{stat} \simeq 3.8\%,$$

$$ZH \rightarrow q\bar{q}H : \quad (\Delta M_H)_{stat} \simeq 50 \text{ MeV}, \quad \left(\frac{\Delta g_{ZZH}}{g_{ZZH}} \right)_{stat} \simeq 0.7\%,$$

assuming $\int \mathcal{L} dt = 500 \text{ fb}^{-1}$ of integrated luminosity.

6 Acknowledgements

The author would like to thank the organizers of the LCWS99 meeting at Sitges for the pleasant setting and stimulating atmosphere provided. The author is also grateful to Dr. Hugh E. Montgomery for reading this manuscript and the constructive criticism provided. This work has been supported by the U.S. Department of Energy under contract number DE-AC02-76CH03000.

References

- [1] S.L. Glashow, Nucl. Phys. **B22** (1961) 579;
S. Weinberg, Phys. Rev. Lett. **19** (1967) 1264;
A. Salam, *Elementary Particle Theory*, ed. N. Svartholm, Almqvist and Wiksell, Stockholm (1968) 367;
S.L. Glashow, J. Iliopoulos and L. Maiani, Phys. Rev. **D2** (1970) 1285.
- [2] H. Murayama and M.E. Peskin, hep-ex/9606003, June 10, (1996).
- [3] J. Ellis, M.K. Gaillard, D.V. Nanopoulos, Nucl. Phys. **B106** (1976) 292;
J.D. Bjorken, Proc. SLAC Summer Institute, 1976;
B. Ioffe, V. Khoze, Sov. J. Part. Nucl. Phys. **9** (1978) 50;
B.W. Lee, C. Quigg, H.B. Thatcher, Phys. Rev. **D16** (1977) 1519.
- [4] D.R.T. Jones, S.T. Petcov, Phys. Lett. **84B** (1979) 440;
R.N. Cahn, S. Dawson, Phys. Lett. **136B** (1984) 196;
G. Altarelli, B. Mele, F. Pitolli, Nucl. Phys. **B287** (1987) 205.
- [5] The LEP Collaborations, CERN-EP-99-015.
- [6] ALEPH 99-081 CONF 99-052; DELPHI 99-142 CONF 327;
L3 Note 2442; OPAL Technical Note TN-614.
- [7] A. Djouadi, hep-ph/99010449, October 22, (1999).
- [8] P. Janot in *Physics and Experiments with Linear e^+e^- Colliders*, Harris F.A., Olsen S.L., Pakvasa S. and Tata X., eds. (World Scientific, Singapore, 1993).
- [9] T. Sjöstrand, Comp. Phys. Com. **82** (1994) 74.
- [10] T. Ohl, hep-ph/9607454-rev, July 1996 (expanded September 1996).
- [11] M. Pohl and H.J. Schreiber, DESY Preprint DESY 99-01, January 1999.
- [12] Webpage for the Model Detectors of the USA/Canada Linear Collider Detector Simulation Group: “<http://www.slac.stanford.edu/~mpeskin/LC/modeld.html>”.
- [13] T. Behnke, G. Blair, K. Mönig and M. Pohl, November 8, (1998),
“<http://www.hep.ph.rhbnc.ac.uk/~blair/detsim/brahms.html>”.
- [14] D. Brown and M. Frank, ALEPH 92-135 PHYSIC 92-124.
- [15] P. García-Abia and W. Lohmann, hep-ex/9908065, August 30, (1999).
- [16] Ll. Garrido, S. Gómez, A. Juste and V. Gaitan, Comp. Phys. Com. **104** (1997) 37.
- [17] W. Bartel *et al.* (JADE Collaboration), Z. Phys. **C33** (1986) 23.
- [18] T. Sjöstrand, Comp. Phys. Com. **22** (1983) 227.

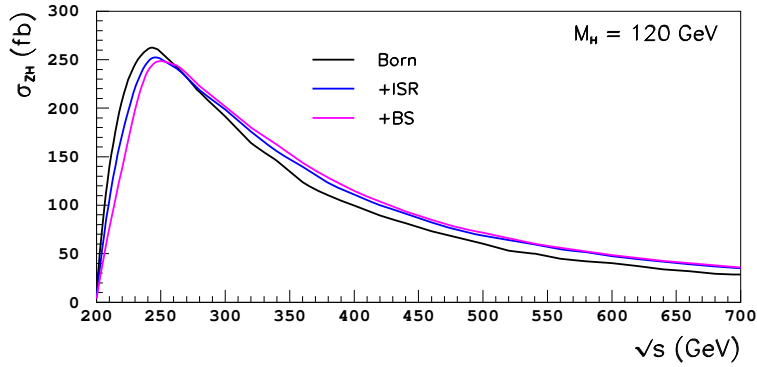


Figure 1: Total cross-section for ZH at lowest order, for $M_H = 120$ GeV, as a function of the center-of-mass energy. The effect of initial state radiation and beamstrahlung on the total cross-section is also illustrated.

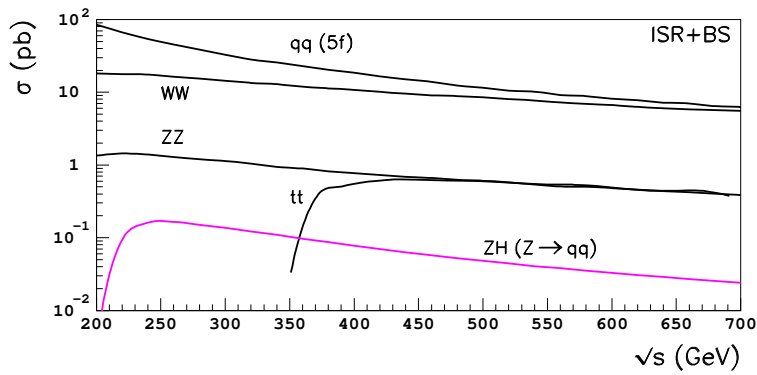


Figure 2: Total cross-section for $ZH \rightarrow q\bar{q}H$ at lowest order, for $M_H = 120$ GeV, and the main background processes considered, as a function of the center-of-mass energy. Initial state radiation and beamstrahlung have been included.

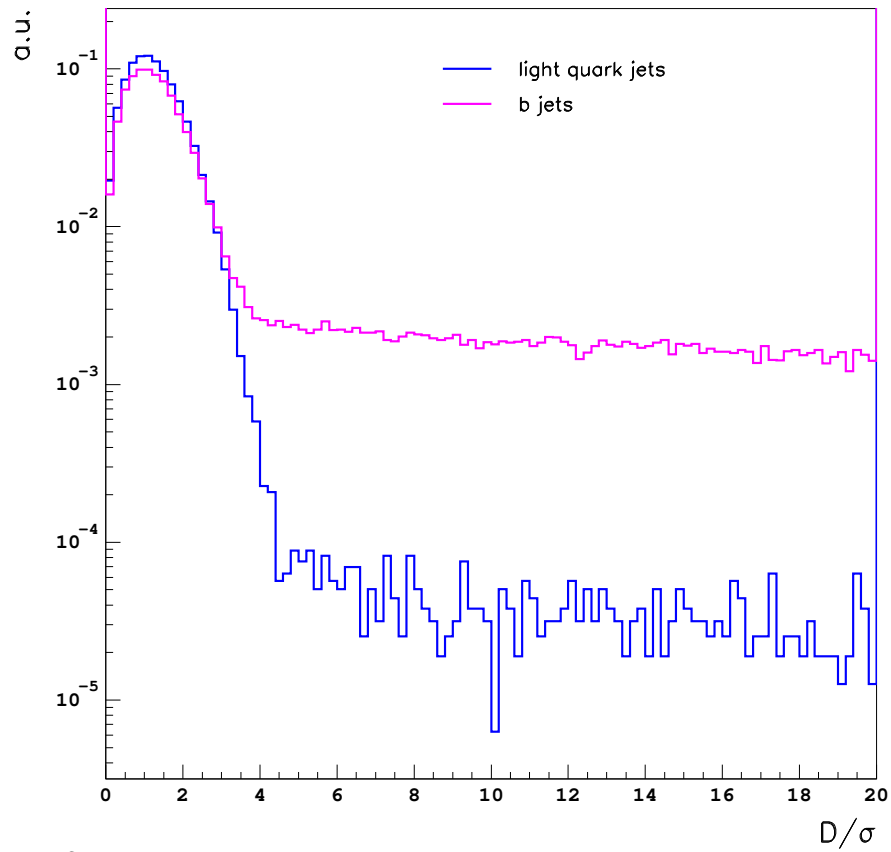


Figure 3: Track 3D impact parameter significance for Z hadronic events at $\sqrt{s}=200$ GeV.

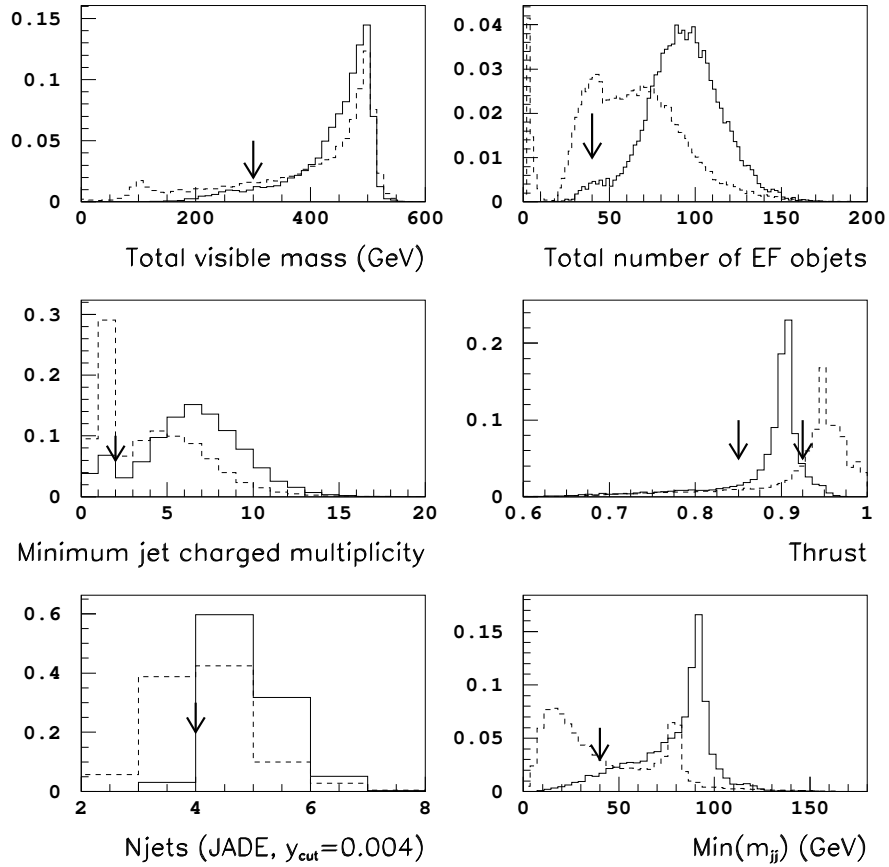


Figure 4: Preselection variables for the hadronic decay channel. Signal (solid) and background (dashed) have been normalized to the same number of events. The background prediction has been computed by adding all the different background contributions weighted according to their relative cross-section.

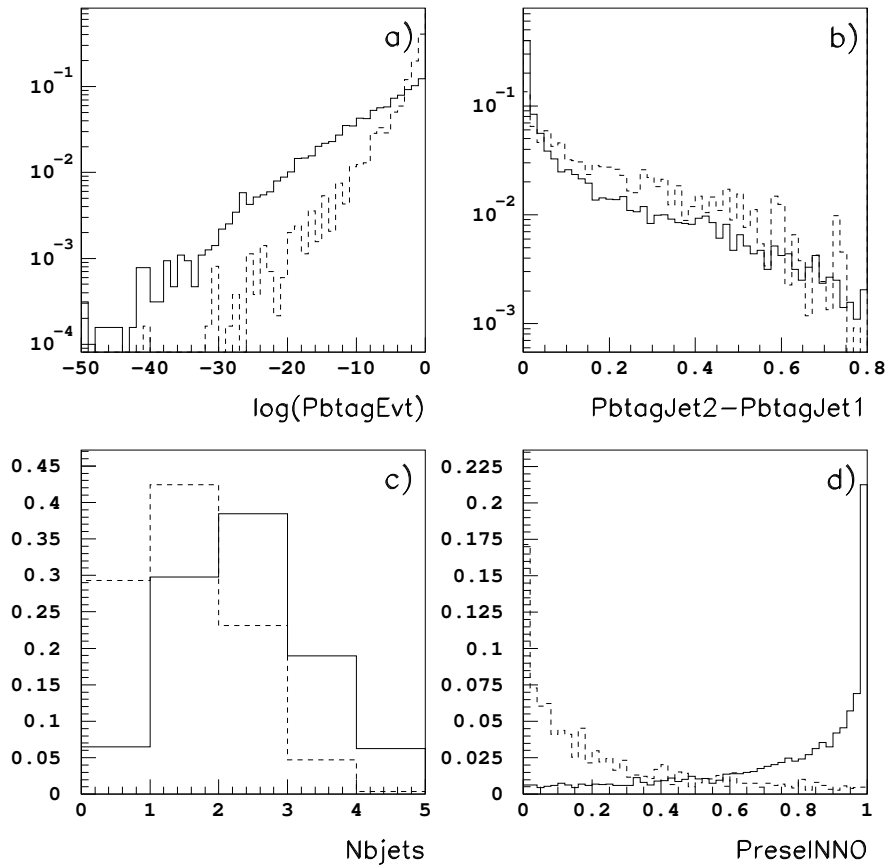


Figure 5: Flavor tagging variables: a), b) and c), used together with the preselection variables to train the Preselection NN, whose output is shown in d). Signal (solid) and background (dashed) have been normalized to the same number of events. The background prediction has been computed by adding all the different background contributions weighted according to their relative cross-section.

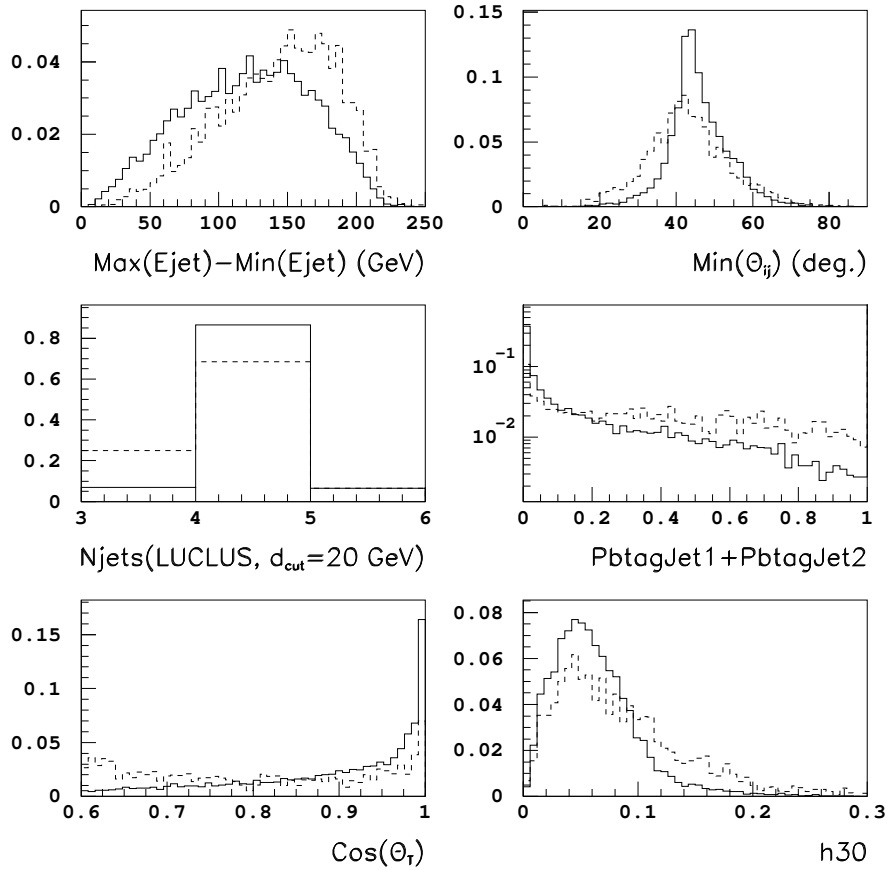


Figure 6: Selection NN variables for the hadronic decay channel (I). Signal (solid) and background (dashed) have been normalized to the same number of events. The background prediction has been computed by adding all the different background contributions weighted according to their relative cross-section.

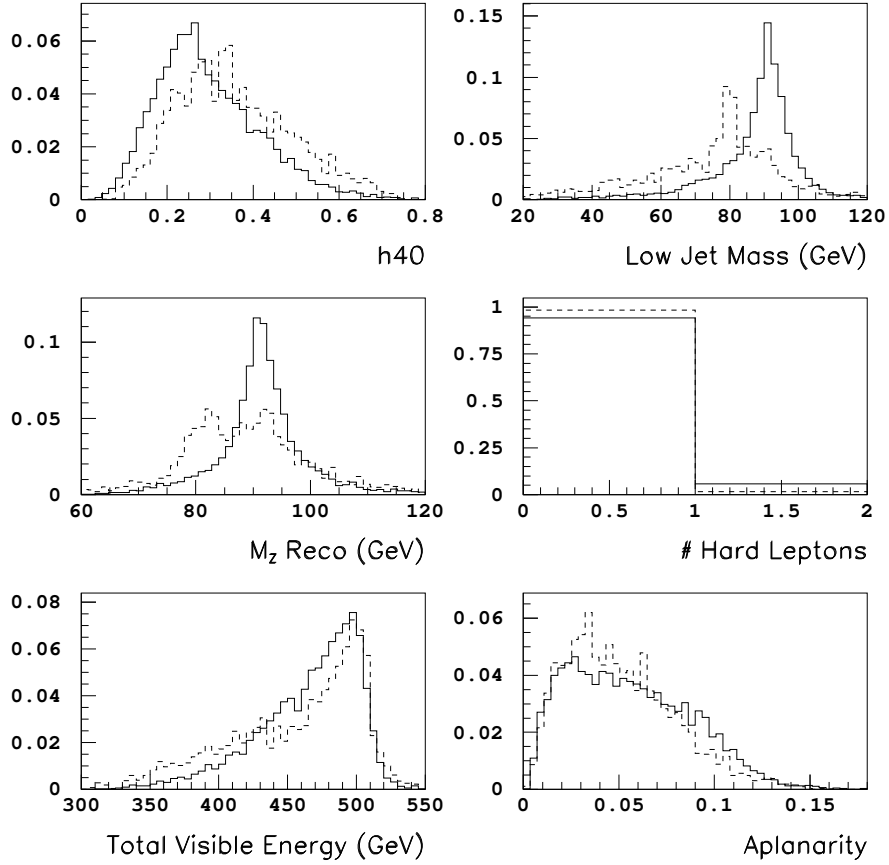


Figure 7: Selection NN variables for the hadronic decay channel (II). Signal (solid) and background (dashed) have been normalized to the same number of events. The background prediction has been computed by adding all the different background contributions weighted according to their relative cross-section.

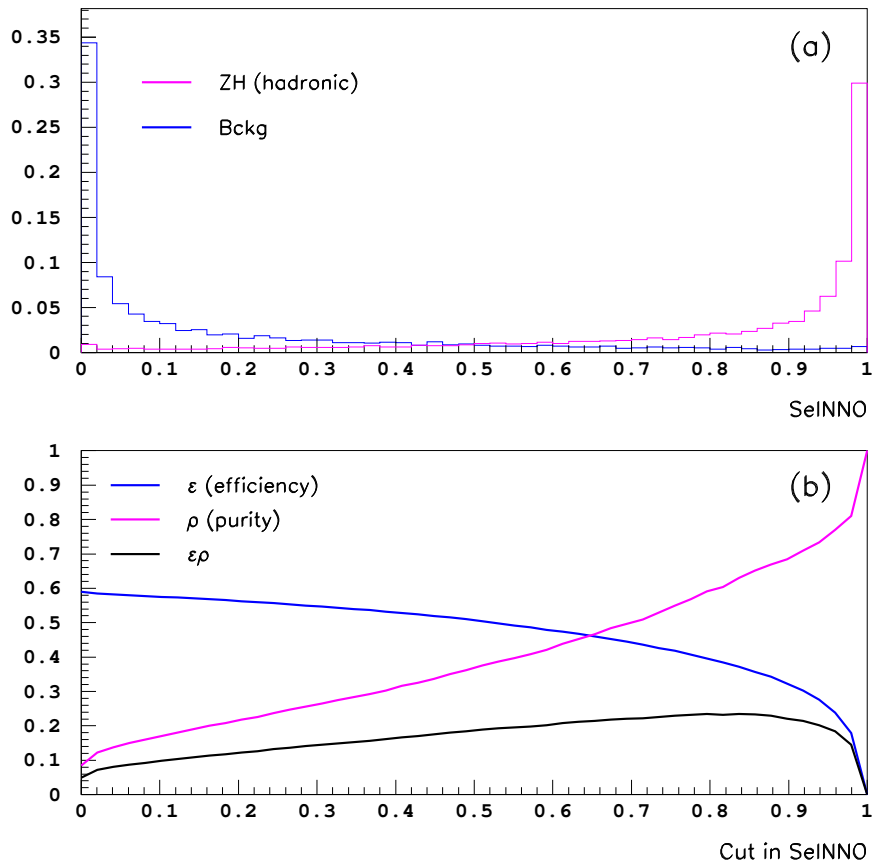


Figure 8: (a) Selection NN output. Signal (purple) and background (blue) have been normalized to the same number of events. (b) Efficiency and purity as a function of the cut in the Selection NN output.

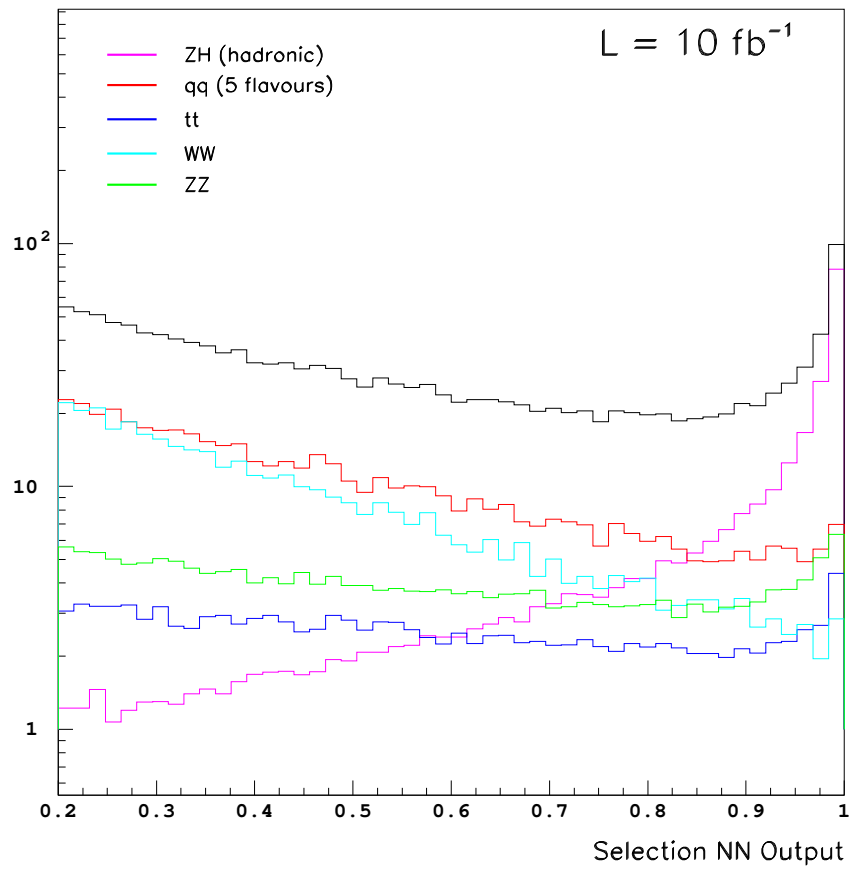


Figure 9: Selection NN output. For the sake of clarity, the NN output is restricted to be larger than 0.2. The different contributions have been normalized to the same integrated luminosity.

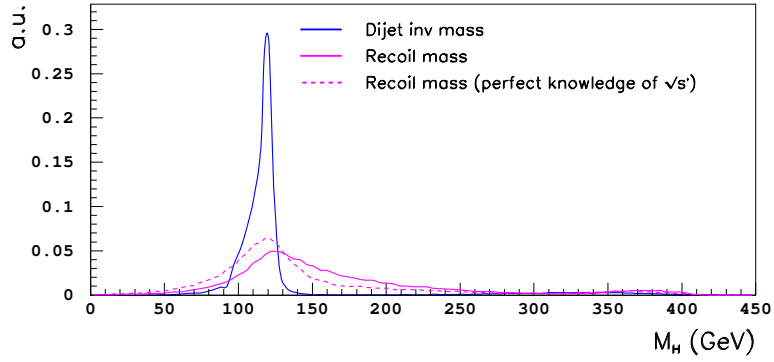


Figure 10: Comparison between the raw H di-jet invariant mass and recoil mass distributions. A selection cut of $\text{SelNNO} > 0.9$ has been applied but no background has been included. All distributions have been normalized to the same number of events.

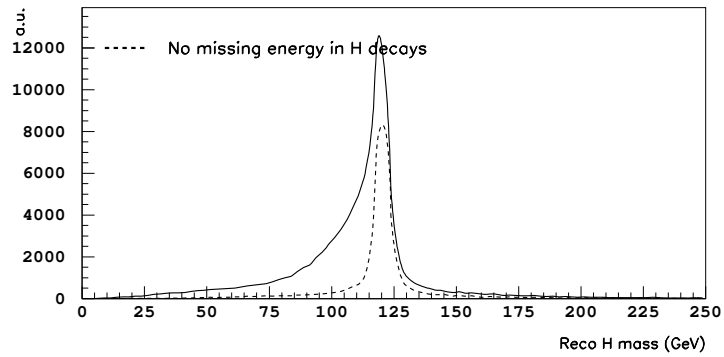


Figure 11: Raw H di-jet invariant mass distribution. The contribution from events with missing energy below 2% shows a sharp and symmetric distribution around 120 GeV (dashed). No background has been included.

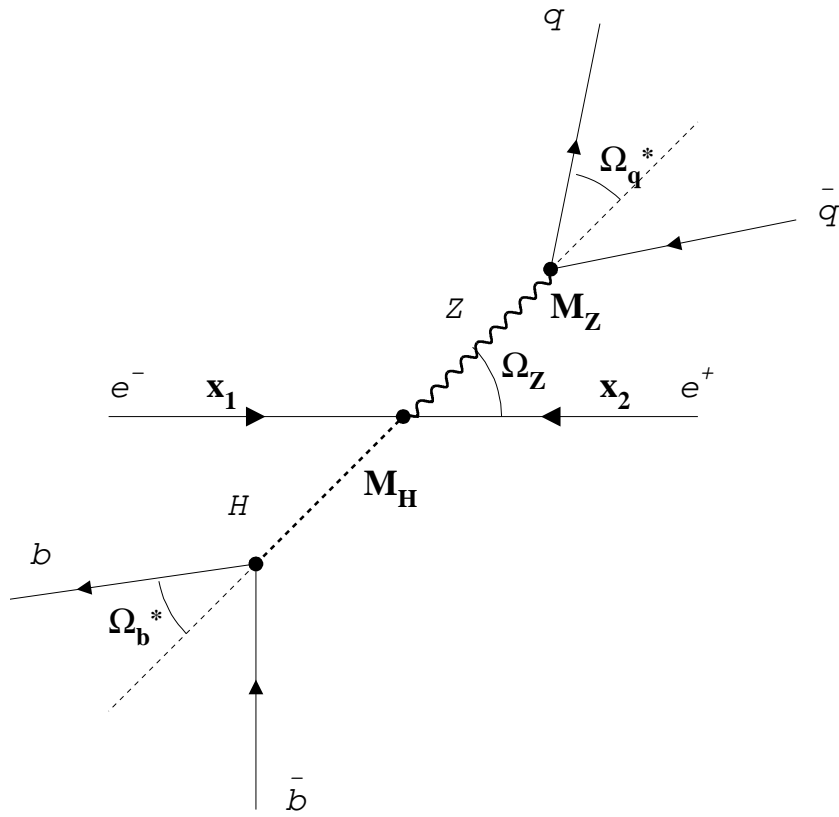


Figure 12: Set of kinematical variables to describe ZH production. The angular variables are generically denoted by $\Omega = (\theta, \phi)$.

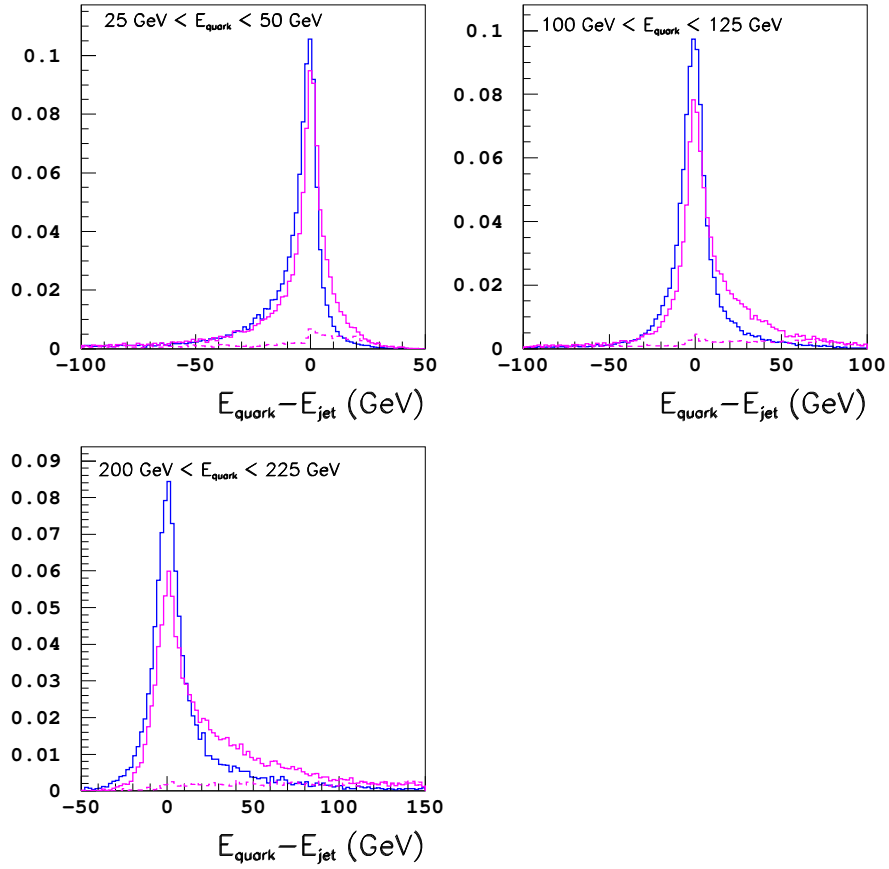


Figure 13: Jet energy resolution for light-quark jets (from Z decays, blue solid histogram) and “ b -jets” (from H decays, magenta solid histogram) in different parent quark energy ranges. The contribution from $H \rightarrow W^+W^-, \tau^+\tau^-$ decay channels is also explicated (magenta dashed histogram).

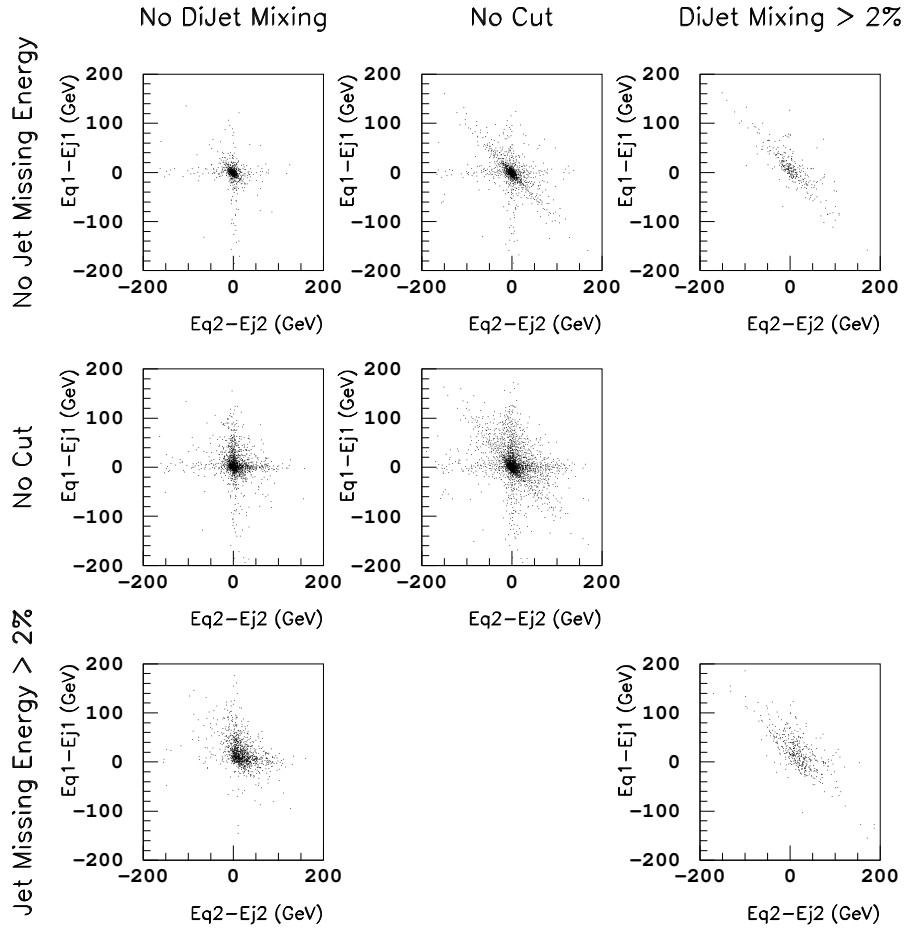


Figure 14: Effect of jet-mixing and energy losses on the bi-dimensional distribution of energy resolution for both H jets. Only $H \rightarrow b\bar{b}, c\bar{c}, gg$ decay channels have been included.

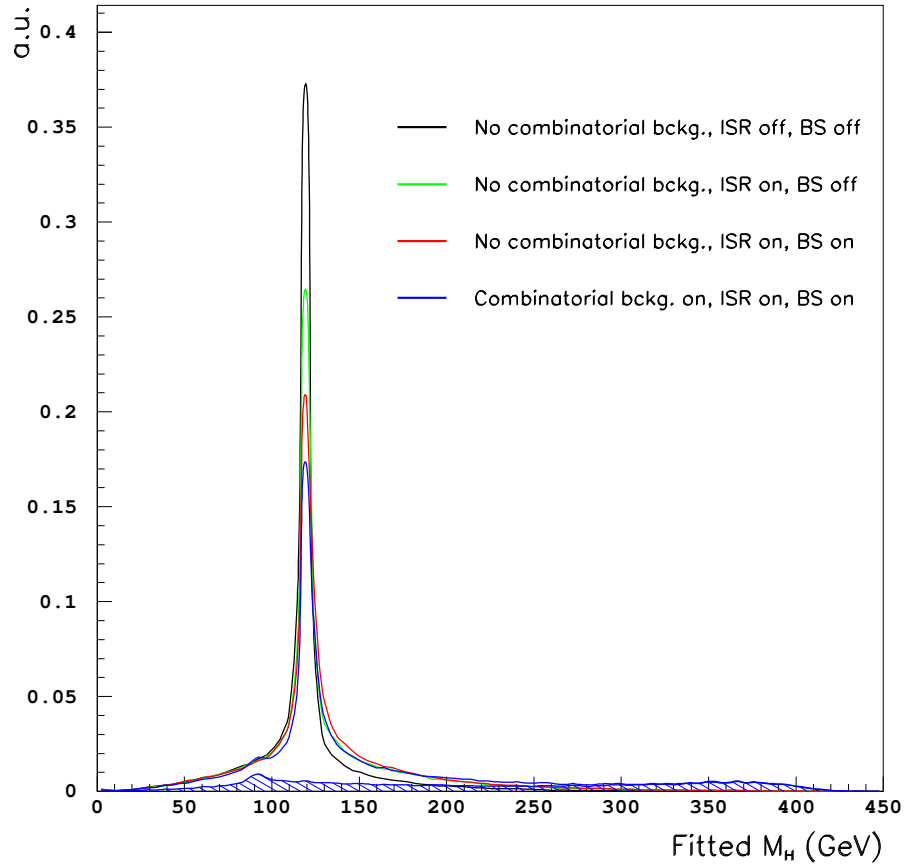


Figure 15: Effect of initial state radiation (ISR), beamstrahlung (BS) and combinatorial background on the fitted Higgs invariant mass. ISR and BS are not taken into account in the kinematical fit. The shaded histogram shows the contribution from the combinatorial background. All distributions have been normalized to the same number of events.

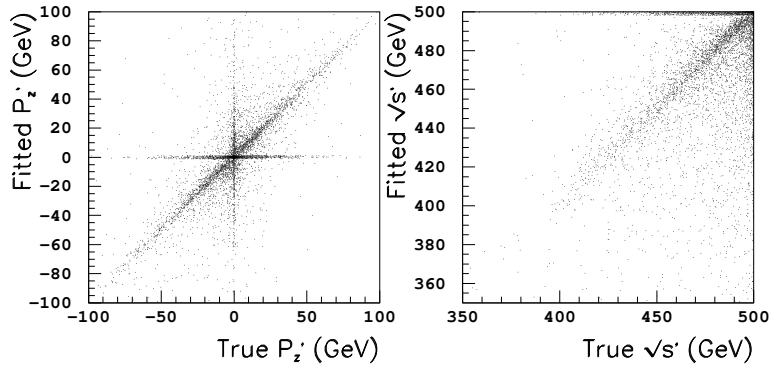


Figure 16: True versus fitted total longitudinal momentum (left) and effective center-of-mass energy (right).

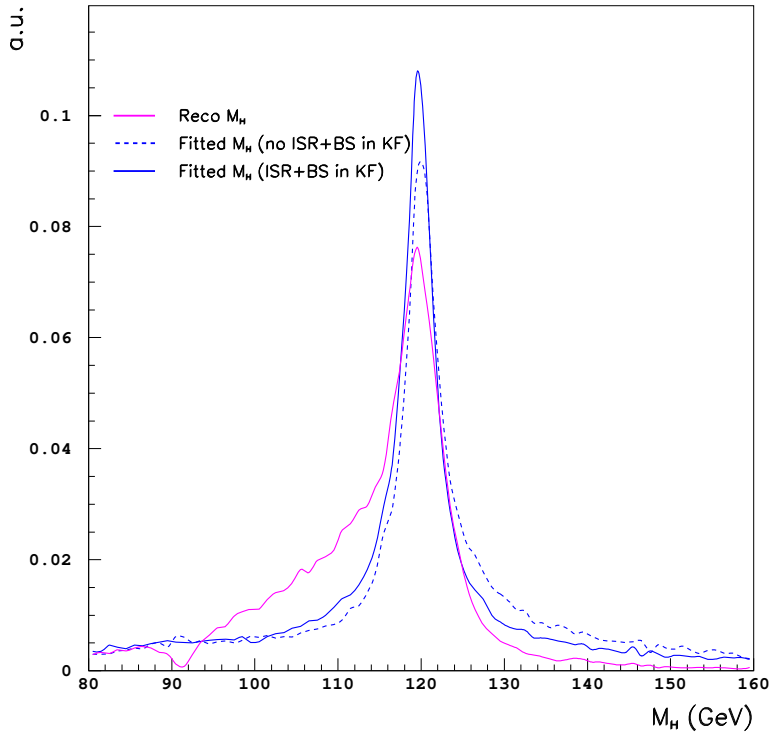


Figure 17: Comparison between raw reconstructed (magenta) and fitted Higgs invariant mass distribution (blue). The improvement by including ISR and BS in the kinematical fit is clearly observed. No background has been included.

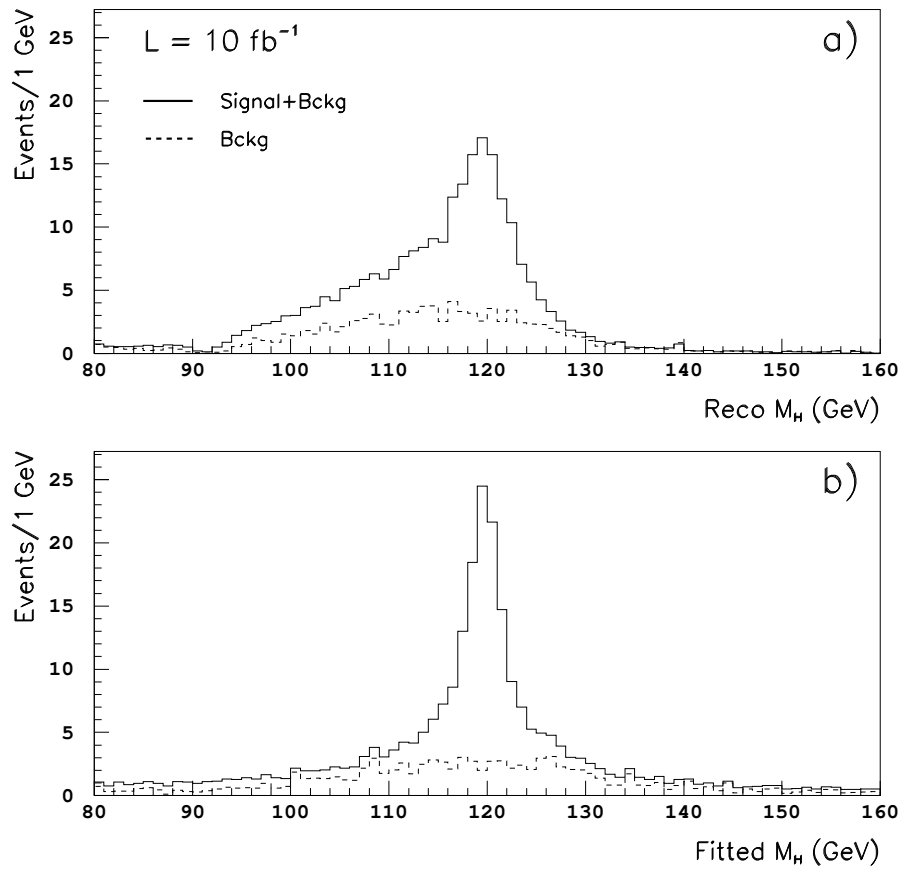


Figure 18: Higgs invariant mass distribution corresponding to $L = 10 \text{ fb}^{-1}$ and including background (dashed): (a) raw reconstructed di-jet invariant mass, (b) di-jet invariant mass from the kinematical fit taking into account ISR and beamstrahlung.